



Prediction of overcharge-induced serious capacity fading in nickel cobalt aluminum oxide lithium-ion batteries using electrochemical impedance spectroscopy

Norihiro Togasaki^{**}, Tokihiko Yokoshima, Yasumasa Oguma, Tetsuya Osaka^{*}

Research Organization for Nano and Life Innovation, Waseda University, 513 Waseda-tsurumaki-cho, Shinjuku-ku, Tokyo, 162-0041, Japan

HIGHLIGHTS

- EIS analysis can predict overcharge-induced capacity fade in lithium-ion cells.
- Lithium-ion cells under overcharge conditions show a two-stage capacity fade.
- Steep drop in the cell capacity during overcharge is due to anode and cathode decay.
- DVA confirms that degradation occurs first at the cathode.
- Metal deposition on the anode can predict serious capacity decay.

ARTICLE INFO

Keywords:

Electrochemical impedance spectroscopy
Lithium-ion battery
Overcharge
Equivalent circuit
Capacity-fading prediction

ABSTRACT

Prediction of degradation in lithium-ion batteries is critical to ensure battery safety. In this study, we report for the first time that electrochemical impedance spectroscopy (EIS) predicts serious capacity fade in lithium-ion batteries, which results from charge-discharge cycling under overcharge conditions. A nickel cobalt aluminum oxide (NCA) lithium-ion cell shows a two-stage capacity fade in the overcharge condition with an upper cutoff voltage (UCV) of 4.4 V. The capacity gradually decreases as cycling progresses (first stage), and then decreases steeply in the later cycles (second stage). Such a two-stage capacity fade is not observed when cell cycling in the appropriate voltage range ($UCV \leq 4.2$ V). In the first stage, the cell capacities cycled at UCVs of 4.2 V and 4.4 V are approximately identical, with an inductively coupled plasma atomic emission spectrometry analysis confirming overcharge-induced deposition of Ni and Co on the anode surface. EIS analysis is used to model these deposited metals as enhanced impedance signals that represent the charge transfer resistance and interfacial capacitance of the anode in the first stage. This allows the advance prediction of overcharge-induced serious capacity decay in lithium-ion batteries to prevent cell destruction.

1. Introduction

Lithium-ion batteries that exhibit high power and energy densities are being widely used in electric vehicles (EVs), as recent efforts to establish a sustainable energy society have focused on reducing energy consumption. Recent improvements in the battery materials and their appropriate selection have increased the energy density of the battery modules (or packs), resulting in the EVs having a longer driving range [1,2]. Safety is an important prerequisite for practical applications, in addition to improvements in the battery performance. Operation of the

batteries under harsh conditions might cause the sudden release of high-dense chemical energy in the form of fire or explosions [3].

Overcharge is a harsh condition wherein the lithium-ion cells in the EVs tend to be potentially exposed. Lithium-ion cells in a battery module, which are connected in series, are controlled using an overall voltage protocol during battery operation. This might cause a few cells in the battery module to experience overcharge, unless each cell has the same capacity and state of charge (SOC) during operation [4]. Overcharge causes detrimental problems in lithium-ion cells such as the deformation of the cathode active materials, oxidation of electrolytes,

* Corresponding author.

** Corresponding author.

E-mail addresses: n-togasaki@ruri.waseda.jp (N. Togasaki), osakatets@waseda.jp (T. Osaka).

<https://doi.org/10.1016/j.jpowsour.2020.228168>

Received 26 July 2019; Received in revised form 6 February 2020; Accepted 6 April 2020

Available online 18 April 2020

0378-7753/© 2020 The Authors. Published by Elsevier B.V. This is an open access article under the CC BY license (<http://creativecommons.org/licenses/by/4.0/>).

and lithium metal deposition on the anode, resulting in serious capacity deterioration [5,6]. Capacity deterioration in an individual cell further promotes overcharge and the phenomena mentioned above, which could trigger either thermal runaway, fire, or explosions [3]. Thus, the prediction of overcharge-induced capacity deterioration is critical to ensure battery safety.

Electrochemical impedance spectroscopy (EIS) is an effective method for evaluating the internal status of a battery cell without causing destruction. A small voltage or current signal is loaded/applied to a battery cell, and the output signal is analyzed using an appropriate equivalent circuit. This allows the separation of the electrochemical reactions that occur in a battery cell into elementary processes based on different time constants and enables the quantitative evaluation of battery deterioration. We have previously reported a technique to effectively distinguish the time constant of each elementary process based on its temperature dependence [7], and proposed an appropriate equivalent circuit that incorporates the particle size distribution of the active electrode materials in commercial batteries [8]. We have also reported the analytical EIS measurement results of battery degradation in commercial batteries resulting from charge–discharge cycling [9,10].

In this study, we investigate the effect of charge–discharge cycling under overcharge conditions on the capacity of lithium-ion batteries and analyze the battery degradation using EIS measurement. Battery degradation was also evaluated using differential voltage analysis (DVA) [11], inductively coupled plasma atomic emission spectrometry (ICP-AES), and Lithium-7 nuclear magnetic resonance (^7Li -NMR) measurement. We show that overcharge-induced serious capacity decay in a lithium-ion battery can be predicted analytically in advance by analyzing the enlarged EIS signals from anode metal deposition, which resulted from the dissolution of the cathode materials.

2. Experimental

High-energy Panasonic NCR18650PF cells with a capacity of ca. 2.9 Ah were used throughout this study. The anode and cathode in the cell are composed of graphite and nickel cobalt aluminum oxide (NCA), respectively (Supplementary Fig. S1). This battery should be operated below 4.20 V based on the product specifications.

The charge–discharge test was performed using a battery-testing instrument (HJ1010SM8A, Hokuto Denko) with a lower cutoff voltage (LCV) of 3.47 V (SOC20%) and an upper cutoff voltage (UCV) of 3.96 V (SOC80%), 4.20 V (SOC100%), 4.30 V (SOC104%), or 4.40 V (SOC107%). The test was conducted using a constant-current/constant-voltage (CC–CV) protocol, with a charging and discharging load current of 1.45 A (0.5 C rate) and 2.90 A (1.0 C rate), respectively. The termination current was set to 0.1 A. This implies that the cell was charged or discharged to the UCV or LCV, respectively, and the voltage was maintained till the current dropped to 0.1 A. After 0–400 charge–discharge cycles, the cell capacity was obtained by subjecting the battery cells to one cycle in the 3.00 V–4.20 V voltage range. This measurement was performed using a CC–CV sequence with constant and cutoff currents of 0.29 A and 0.029 A, respectively.

The impedance spectra of the battery cells were measured using a potentiostat (CellTest System 1470E, Solartron) and frequency analyzer (CellTest System 1400, Solartron) at the open circuit voltage, with a 10 mV (zero to peak) ac signal in a frequency range of 10 kHz to 10 mHz. The cell voltage for the impedance measurement was set to 4.20 V (SOC100%). The impedance measurement for the pristine cell was performed at different temperatures of -20°C , 0°C , 25°C , and 45°C to evaluate the elemental processes in the cell. Data fitting was performed using the Microsoft Excel Solver package until the minimum error was obtained. This was achieved by minimizing the sum of all differences between the acquired experimental complex impedance data and calculated impedances from the equivalent circuit using the fitted parameters at each frequency, similar to the procedure detailed in our previous reports [8–10].

The capacities of the anode and cathode and utilization of the two electrodes (electrode balancing) were determined using DVA [11–13]. The voltage slope at open circuit holds information on the anode and cathode active materials present in the cell, because the cell voltage at open circuit depends on the electrochemical potential difference between the anode and cathode. Bloom et al. [11] established that the dV/dQ peak obtained from the voltage slope represents the phase transitions of the anode or cathode active materials. For the battery cell used in this study, a significant voltage change at the LCV is associated with the increasing potential of the graphite anode. This indicates that the partial anode capacity can be observed between the peak voltage of dV/dQ (derived from the anode) and LCV. Similarly, the partial cathode capacity can be observed between the peak voltage of dV/dQ (derived from cathode) and UCV, as a significant change in the UCV is associated with the NCA cathode. Information on the electrode balancing is represented by the capacity between the dV/dQ peak derived from the anode and that from the cathode. In this study, a small charging current of 0.1 A (ca. 0.034 C rate) was loaded/applied to the battery cell in a voltage range of 2.50–4.20 V to obtain a quasi-open circuit potential profile.

The inductively coupled plasma atomic emission spectrometry (ICP-AES) chemical analysis (SPS-3520, SII Nano Technology) was performed to quantify the metal deposits on the anode surface. The graphite anode was first transferred from the 18650 type cylindrical cell to the Ar filled glove box. This was then washed with dimethyl carbonate to remove the residual electrolyte, dried, scraped off the copper current collector, and incinerated. The resultant ash was dissolved in a strong acid and diluted with water for analysis.

The ^7Li -NMR technique was used to detect the presence (or absence) of metallic lithium on the graphite anode. Solid-state MAS NMR measurement was performed using a Bruker AVANCE III 600 MHz spectrometer (14.1 T, ^7Li Larmor frequency = 233.23 MHz) equipped with a 4.0 mm MAS probe head. Data were collected using a single pulse with a pulse length of 1.4 μs , and the spinning speed was 15 kHz. The chemical shift of lithium cobalt oxide (-0.5 ppm) was used as the reference.

3. Results and discussion

Fig. 1 shows the charge and discharge capacities of the NCA lithium-ion cell following cycling in the voltage ranges 3.47 V–4.20 V (UCV 4.20 V) and 3.47 V–4.40 V (UCV 4.40 V). The charge and discharge capacities gradually decrease in proportion to the square root of the cycle numbers ($\approx -11 \text{ mAh}/\sqrt{\text{Cycle Number}}$) when cycling at an UCV of

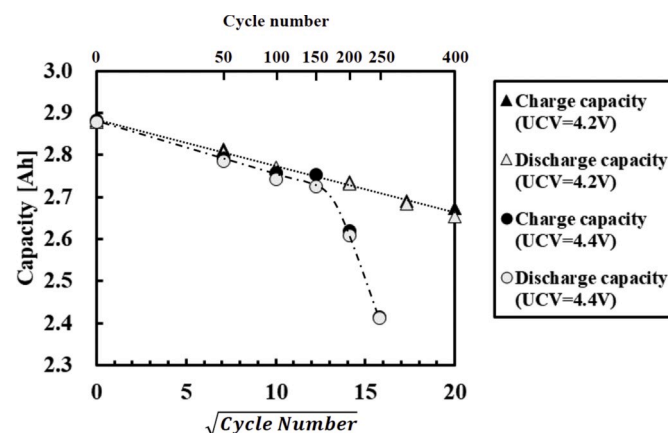


Fig. 1. Charge or discharge capacity fade of the battery cells, which were cycled in voltage ranges of 3.47 V–4.20 V (UCV 4.20 V) and 3.47 V–4.40 V (UCV 4.40 V). “UCV” refers to the upper cutoff voltage during charge–discharge cycling. The charge or discharge capacity was measured in the voltage range of 3.00 V–4.20 V using the CC–CV mode with constant and cutoff currents of 0.29 A and 0.029 A, respectively.

4.20 V. This phenomenon was observed because the formation or growth of the solid electrolyte interphase (SEI) on the graphite anode [14,15] or degradation of the cathode materials [9] leads to a decrease in the lithium inventory. The battery cell shows a two-stage capacity fade when an UCV of 4.40 V causes an overcharge. The capacity decreases gradually initially as the cycling progresses (first stage ≤ 150 cycles), and subsequently experiences a steep decrease in the later cycles (second stage >150 cycles). During the first stage, the cell capacities cycled at the UCVs of 4.20 V and 4.40 V are nearly identical, whereas the cell capacity cycled at an UCV of 4.40 V decreases steeply during the later cycles in the second stage ($\approx -85 \text{ mAh}/\sqrt{\text{Cycle Number}}$). Supplementary Fig. S2 shows that such two-stage capacity fades are only observed when the charge–discharge cycling is performed under overcharge conditions ($\text{UCV} \geq 4.3 \text{ V}$). Thus, the significant drop in the capacity during the second stage can be attributed to the battery degradation from overcharging.

The results discussed above indicate that the UCV during charge–discharge cycling affects the capacity deterioration characteristics of the cell. The capacity deterioration of the lithium-ion batteries can be classified into three degradation modes, namely, the loss of the cathode and anode active materials, and lithium inventory [16]. The lithium inventory refers to the amount of lithium that can move between the anode and cathode in a certain voltage range, which is determined by the electrode balancing between the anode and cathode. The lithium inventory changes when side/peripheral reactions occur on the anode or cathode. The inventory decreases when side reactions such as electrolyte reduction or SEI growth occur on the anode, whereas it increases when side reactions such as electrolyte oxidation occur on the cathode [12]. The deterioration of the anode or cathode active materials such as structural deformation or electrical isolation leads to a loss of active electrode materials. We performed DVA on the cycled battery cells to investigate the effects of overcharge during charge–discharge cycling on the lithium inventory and capacity of the anode or cathode active materials in the cell. In DVA, a small current that is typically less than 0.05 C was loaded to the cell to obtain a quasi-open circuit voltage profile for the conversion of dV/dQ . This was subsequently analyzed as a function of the cell or electrode capacity to evaluate the amount of charge in the lithium inventory or electrode materials in the cell. Fig. 2 shows the dV/dQ profile plotted as a function of the cell capacity

obtained from a pristine cell. A charging current of 0.1 A (0.034 C) was applied to the cell in the 2.50 V–4.20 V voltage range (left to right in the figure). The figure shows several marked peaks in the dV/dQ curve, with rapid transitions seen at the initial and final points. The results from a cell containing the lithium-based graphite anode and NCA cathode (Supplementary Fig. S3) show the dV/dQ peaks or slopes derived from the phase transitions of the graphite anode or NCA cathode (Fig. 2). The “A” and “C” points in Fig. 2 correspond to the graphite anode and NCA cathode, respectively. The capacity of Q_A depends only on the anode characteristic (partial capacity of anode). In other words, Q_A contains information on the anode capacity. Similarly, the capacity of Q_C depends only on the cathode characteristic (partial capacity of cathode), which incorporates information on the cathode capacity. The capacity of Q_B represents the charge between the cathode and central anode peaks, containing information on both the anode and cathode. This suggests that Q_B is a good indicator of the electrode balancing between the anode and cathode. Q_T represents the total capacity of the cell in the 2.50 V–4.20 V voltage range.

Following the procedure mentioned above, the capacities corresponding to Q_A , Q_B , Q_C , and Q_T obtained from the cycled battery cells are shown in Fig. 3. The battery cells were cycled in the 3.47 V–4.20 V (UCV 4.20 V) and 3.47 V–4.40 V (UCV 4.40 V) voltage ranges. The result of Q_T is similar to that seen in Fig. 1. The capacity of the cell cycled at an UCV of 4.20 V decreases constantly in proportion to the square root of the cycle numbers, while a two-stage capacity fade can be observed at an UCV of 4.40 V. This is observed because Q_T describes the total cell capacity during charging. A similar behavior was seen with respect to the capacity in Q_A , which showed a two-stage capacity fade with serious deterioration after 200 cycles when the cell was cycled at an UCV of 4.40 V. This serious anode deterioration could be the result of an overcharge from the deposition of lithium on the graphite surface. Ansean et al. have reported that the capacity deterioration at a steeper rate can be attributed to the side effects of lithium plating in a graphite–lithium iron phosphate battery [17]. Considering the above, we performed a ^7Li -NMR analysis for the graphite surface obtained from a cell, which was cycled at an UCV of 4.40 V, after 250 cycles. However, no signal from the metallic lithium, which should be observed around 265 ppm, was detected (Supplementary Fig. S4) [18]. This indicates the existence of another mechanism that accounts for the steeper capacity fade in interval Q_A . There was no significant difference in Q_C up to a 100 cycles regardless of the UCV settings during cycling. Clear differences can be observed in the capacity of Q_C , which was evaluated from the cells cycled at UCVs of 4.20 V and 4.40 V. The capacity fades in Q_A and Q_C show similar trends. However, the capacity difference in Q_C , either in the presence or absence of overcharge, was observed earlier (<200 cycles) as compared to that in Q_A (>200 cycles). The overcharge-induced capacity deterioration of the NCA cathode can be attributed to microstructural changes such as the cracking and electrical isolation of the NCA particles, surface structural changes causing nonionic conducting and electronically insulating phases, or dissolution of the transition metals [19,20]. The capacity in Q_B exhibited different behavior as compared to that in Q_A and Q_C . The capacity in Q_B from the cell cycled at an UCV of 4.20 V remains approximately constant, while Q_B from the cell cycled at an UCV of 4.40 V gradually decreases until 100 cycles and subsequently remains constant. As previously mentioned, the capacity in Q_B represents the electrode balancing between the anode and cathode. It is affected by the side reactions on each electrode. A slight decrease in the capacity in Q_B from the cell cycled at an UCV of 4.40 V suggests that the capacity shift of the graphite anode occurs more readily than that of the NCA cathode [12]. The reason for the behavior of Q_B as a function of cycling number is still under debate.

The DVA results indicate that the capacity deterioration of the cell cycled at an UCV of 4.20 V was mainly due to a gradual capacity decrease of the graphite anode and NCA cathode, because there was no significant change in the electrode balancing. The gradual capacity deterioration until 100 cycles (stage 1) in a cell cycled at an UCV of 4.40

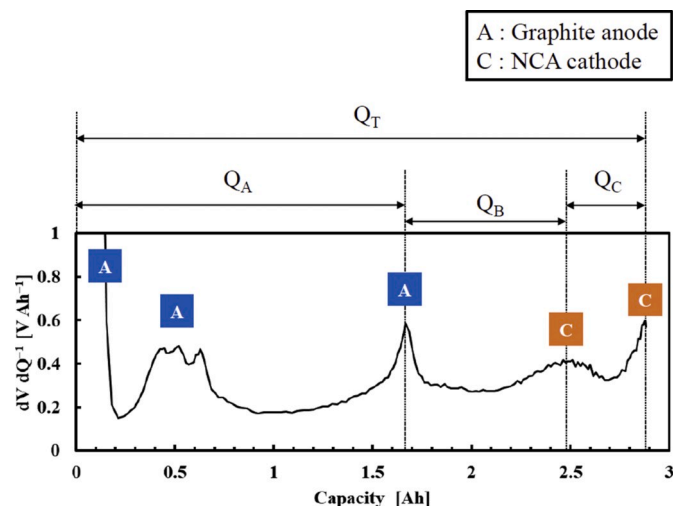


Fig. 2. Differential voltage (dV/dQ) profile of the 18650 cylindrical cell, with a loading current of 0.1 A in the 2.50 V–4.20 V voltage range. Notations A and C refer to the signal corresponding to the graphite anode and NCA cathode, respectively. The graphite anode and NCA cathode capacities can be observed in the Q_A and Q_C , respectively, as they are affected by only each electrode. The capacity of Q_B indicates the electrode balancing between the graphite anode and NCA cathode. The capacity Q_T refers to the total capacity of the cell.

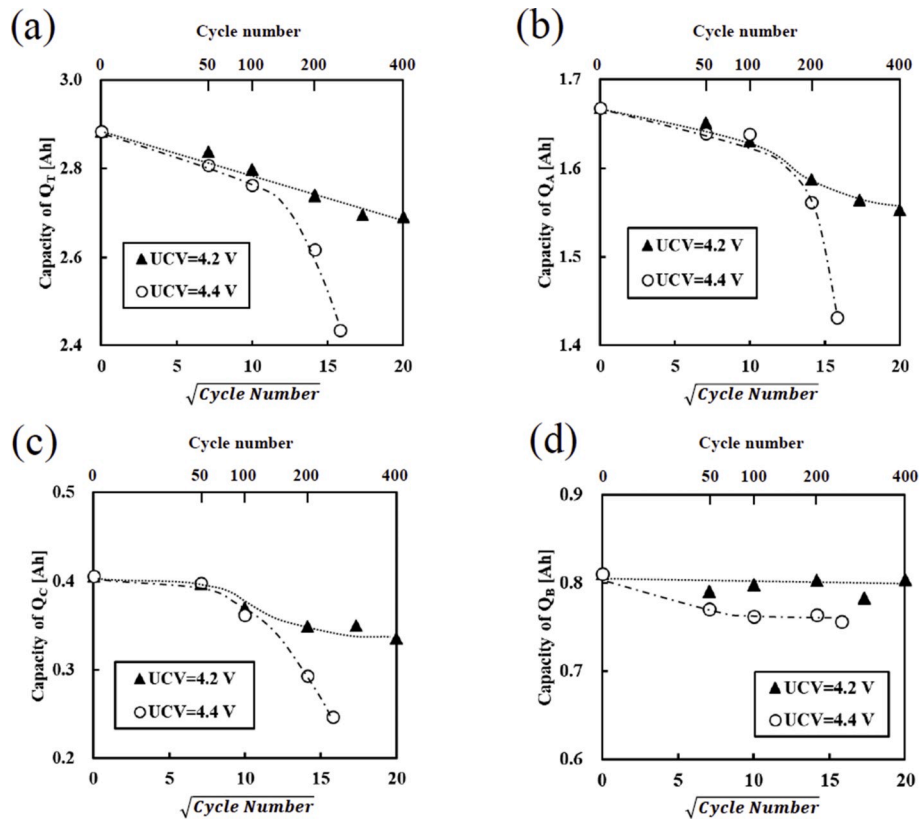


Fig. 3. (a) The total capacity (Q_T) and degradation indicators of the (b) graphite anode (Q_A), (c) NCA cathode (Q_C), and (d) capacity balancing (Q_B) in the NCA cells, which were charge–discharge cycled in the 3.47 V–4.20 V (UCV 4.20 V) and 3.47 V–4.40 V (UCV 4.40 V) voltage ranges.

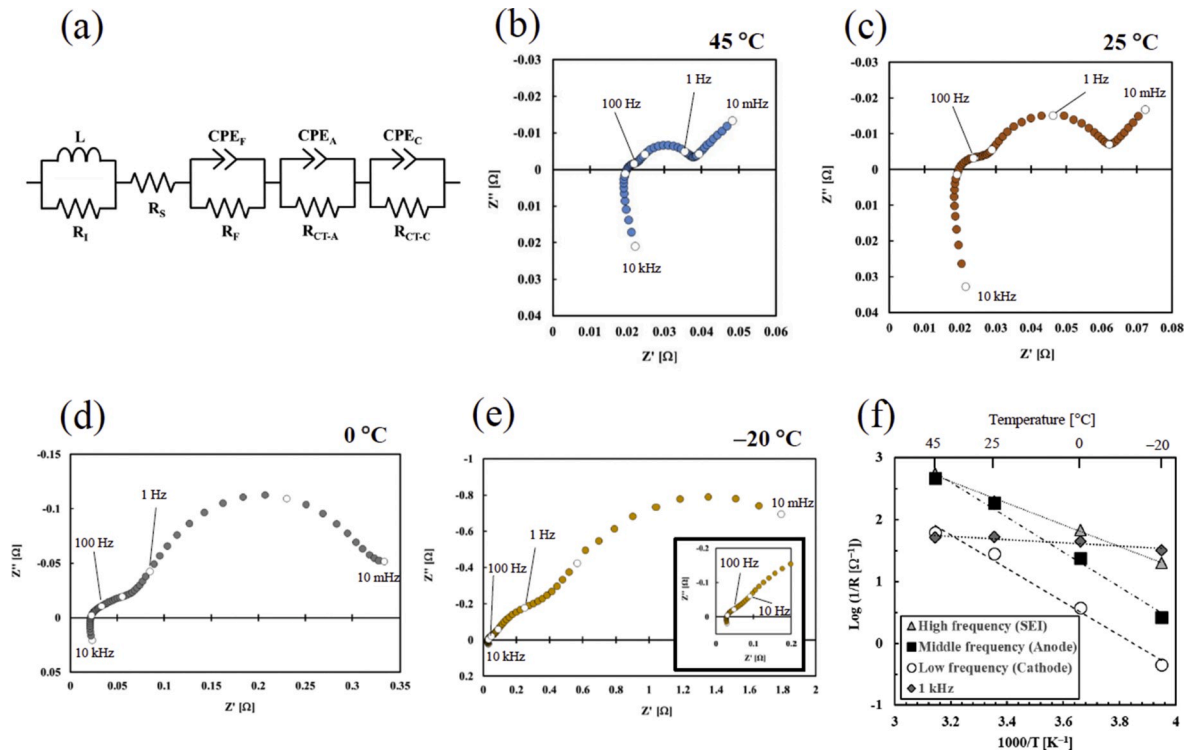


Fig. 4. (a) Equivalent circuit used to analyze the impedance spectra in this study. Notations: L and R_l , inductance and resistance of the battery leads and connected cable, respectively; R_s and R_F , resistance of the electrolyte and SEI, respectively; CPE_F , constant phase element of the SEI; R_{CT-A} and R_{CT-C} , charge transfer resistance of the anode and cathode, respectively; and CPE_A and CPE_C , constant phase element of the anode and cathode electrode surfaces, respectively. Nyquist plots from the battery cell at a temperature of (b) 45 °C, (c) 25 °C, (d) 0 °C, and (e) -20 °C. (f) Arrhenius plots of the three identified elementary processes corresponding to the SEI, graphite anode, and NCA cathode.

V might be due to a gradual decrease in the graphite anode and NCA cathode capacities, along with a small contribution from electrode unbalancing. The capacity drop in the cell cycled at an UCV of 4.40 V (stage 2) can be attributed to a serious capacity decrease of the graphite anode and NCA cathode.

We investigated cell capacity deterioration in the presence or absence of overcharge during charge–discharge cycling using an analytical tool of DVA. Analysis using EIS was performed to investigate the effect of the cell capacity deterioration caused by an overcharge on the elementary electrochemical processes in the cell. Fig. 4 (a) illustrates the equivalent circuit used in this study, which has three RC parallel connections corresponding to the SEI film, anode, and cathode [7]. We included the SEI component in the equivalent circuit because the anode has a low electrochemical graphite potential, which causes SEI formation on the surface due to the reductive decomposition of the electrolyte or lithium salt. A parallel connection of an inductor (L) and resistor (R_i) was added to include the signal and contact resistance from the wiring and measuring equipment, respectively. EIS measurements at different temperatures were performed to identify the elementary reactions in the EIS spectra. Fig. 4 (b)–(e) show the EIS spectra from the cell at temperatures of 45 °C, 25 °C, 0 °C, and –20 °C, respectively. Two capacitive semicircles in the high- and low-frequency ranges can be observed at both temperatures of 25 °C and 45 °C, while three capacitive semicircles in the high-, mid-, and low-frequency ranges were observed at the low temperature of –20 °C. This suggests that there are three inherent elemental electrochemical processes occurring in the cell, with overlap between two of the three processes at higher temperatures. This result is in good agreement with our previous report wherein the hidden capacitive semicircle in the EIS spectra was revealed at low temperature measurements [7]. The Nyquist plots were analyzed using the equivalent circuit shown in Fig. 4 (a). Supplementary Fig. S5 shows the time constant of each elementary process and apex frequencies of the capacitive semicircles in the high-, mid-, and low-frequency regions along with the results of fitting errors (Error $|Z|$ [%]) as a function of input frequency signals. Fig. 4 (f) shows the Log (1/R) dependency of each elementary process on different temperature conditions. It can be observed that the Log (1/R) value obtained from the semicircles in high-, mid-, and low-frequency regions varies linearly with different slopes as a function of temperature. The activation energies (E_A) of the elementary processes can be calculated using the following equation [21]:

$$1/R_i = A \exp(-E_A/RT)$$

where R_i is the resistance derived from the elementary process in a cell, and A , R , and T are the frequency factor, gas constant, and absolute temperature, respectively. The activation energies from the capacitive semicircles in the mid- and low-frequency regions were calculated to be 52.5 and 50.0 kJ mol^{–1}, respectively. Ogumi et al. found that the activation energy for the charge transfer resistance is 50–60 kJ mol^{–1} in the commonly used electrolytes for lithium-ion batteries such as polypropylene carbonate, ethylene carbonate (EC), and EC mixed with dimethyl carbonate [22]. The capacitive semicircle in the low-frequency region can be attributed to the NCA cathode reactions, as the apex frequency of the charge transfer resistance in transition metal oxides was approximately a few hertz (Supplementary Figure S5 (b)) [23]. Lithium intercalation is accompanied by the formation of lithium-graphite intercalation compounds having several stage structures in the graphite anode. The graphite structure in the EIS measurement is a mixed phase of stage-1 and stage-2 because the EIS measurement was performed at a charge of 4.20 V [24]. Jemenez-Gordon et al. reported that the apex frequency of the charge transfer resistance in the graphite electrode appeared around 40 Hz when the EIS measurement for the charged graphite anode was out evaluated at 25 °C [25]. Thus, the capacitive semicircle observed in the mid-frequency region can be attributed to the graphite anode reactions. The activation energy in the high-frequency region was estimated to be 35 kJ mol^{–1}. Very few studies

have focused on the activation energy of the SEIs. Borodin et al. reported the activation energy of the SEI and electrolyte interface to be 40.5–44.4 kJ mol^{–1}, which is relatively lower than that of the charge-transfer resistance of the anode or cathode [26]. Zhang et al. suggested that the SEI activation energies are smaller than that of charge-transfer resistance of anode or cathode in the –20 °C to 20 °C temperature range [27]. The capacitive semicircle in the high-frequency region can be attributed to the SEI reactions, because the apex of the capacitive semicircle corresponding to the SEIs is typically observed at a few hundred hertz [28,29]. In Fig. 4 (b)–(e), all of the impedance plots at 1 kHz is located at close to real axis. It is generally accepted that the impedance at around 1 kHz represents the ohmic resistance in the internal and external of the battery cell in addition to solution resistance. The activation energy of the impedance at 1 kHz, which is much smaller than any other electrochemical elemental processes in the cell, was calculated to be 4.9 kJ mol^{–1}. This trend is similar to the results reported by Zhang et al. [27] and the obtained activation energy was in between the reported value of ohmic resistance (≈ 1 kJ mol^{–1}) [30] and that of solution resistance (< 15 kJ mol^{–1}) [28,30].

The results above confirm that the electrochemical reactions in the EIS spectra can be separated into elementary processes using a fitting analysis with an appropriate equivalent circuit. Fig. 5(a) and (b) show the Nyquist plots from the cell that was cycled in the 3.47 V–4.20 V (UCV 4.20 V) and 3.47 V–4.40 V (UCV 4.40 V) voltage ranges, respectively. The capacitive semicircle in the low-frequency region increases with the cell cycling number for both UCVs of 4.20 V and 4.40 V. This significant increase in the impedance can be attributed to the NCA cathode behavior.

Fig. 6(a) shows the fitting results of the charge transfer resistance of the NCA cathode (R_{CT-C}) cycled at an UCV of 4.20 V and 4.40 V. The R_{CT-C} evaluated from the cell cycled at an UCV of 4.20 V increases in proportion to the square root of the cycle numbers, whereas a two-stage trend was observed at an UCV of 4.40 V. The R_{CT-C} gradually increases up to 50 cycles, with a drastic increase thereafter. This is consistent with the results shown in Fig. 3 (c) except that the EIS results represent the difference between two conditions at a prior cycle number. This might be due to a dissolution of the transition metals, accompanied by the micro- or surface structural changes of the NCA cathode that prevent the intercalation/deintercalation of the lithium ions. The interfacial capacitances of the NCA cathode remain constant regardless of the charge–discharge cycling conditions (Fig. 6 (b)). This suggests that only a few cathode compounds are electrically isolated due to the volumetric changes that occur during the charge–discharge cycles. The surface area of the cathode active materials might cause the charge–discharge cycling to influence R_{CT-C} but not the interfacial capacitance of the cathode. The cathode is composed of active materials, conductive additives, and binders. The surface area of the cathode active materials tends to be much smaller than that of the conductive additives. The NCA surface area has been reported to be at least one-tenth less than that of a conductive additive such as acetylene black [31]. Thus, the interfacial capacitance of the cathode might not be influenced easily by the deterioration of the NCA active cathode material. The behavior of the graphite anode was significantly different in the presence or absence of overcharge, as shown in Fig. 6(c) and (d). The charge-transfer resistance of the anode (R_{CT-A}) remains approximately constant until 400 cycles when cycling with an UCV of 4.20 V. On the contrary, when cycling under overcharge conditions (UCV of 4.40 V), R_{CT-A} steeply increases after 50 cycles and exceeds twice the value recorded for an UCV of 4.20 V at 100 cycles. The interfacial capacitance of the anode also showed significant differences with an opposite trend. The capacitance at an UCV of 4.40 V steeply decreases after 50 cycles and drops below one-fourth of the value recorded at an UCV of 4.20 V. As previously discussed, this phenomenon cannot be attributed to the lithium deposition on the graphite anode. An increase in the volume of the electrically isolated graphite anode due to the volumetric changes during cycling could be a likely mechanism. The electrical dissociation of the

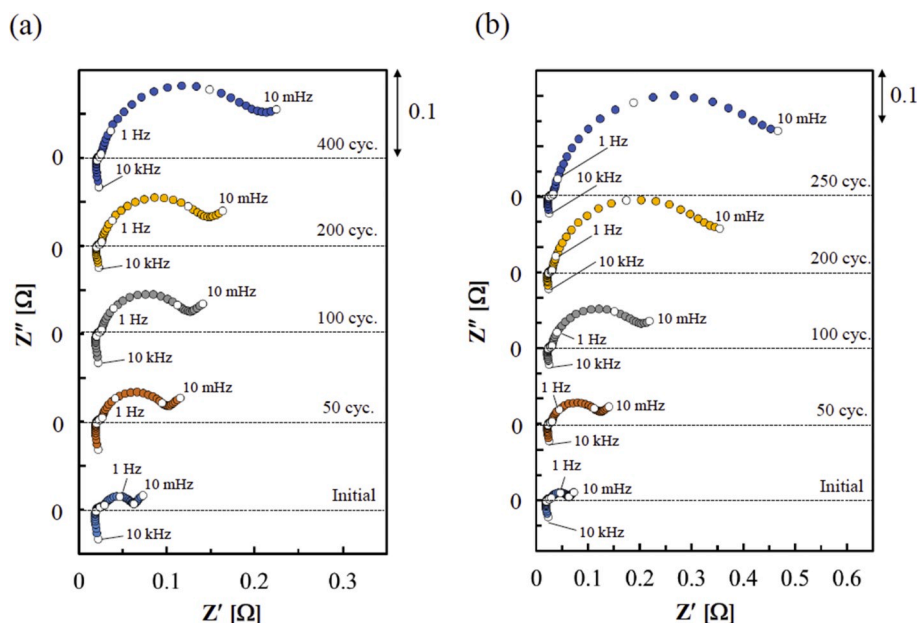


Fig. 5. Nyquist plots from the 18650 cylindrical cells, which were cycled in the (a) 3.47 V–4.20 V (UCV 4.20 V) and (b) 3.47 V–4.40 V (UCV 4.40 V) voltage ranges.

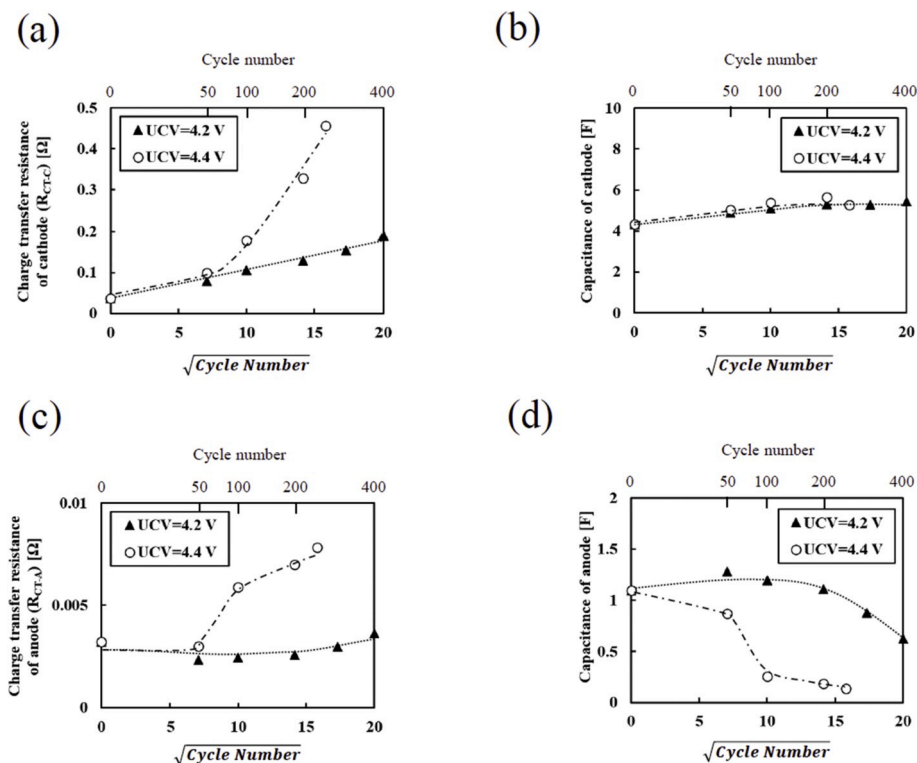


Fig. 6. Fitting results of the (a) charge-transfer resistance (R_{CT-C}) and (b) interfacial capacitance of the NCA cathode, and (c) charge-transfer resistance (R_{CT-A}) and (d) interfacial capacitance of the graphite anode. The battery cells were measured after charge–discharge cycling in the 3.47 V–4.20 V (UCV 4.20 V) and 3.47V–4.40 V (UCV 4.40 V) voltage ranges.

graphite anode from the current collector increases R_{CT-A} as the reaction area reduces, and the interfacial capacitance of the anode decreases as the electrically connected surface area decreases. The impedance analysis results indicate that one-half or more of the anode materials should be electrically isolated by 100 cycles as compared to the initial state, if anode degradation occurs due to dissociation. However, the capacity of the graphite anode after 100 cycles at an UCV of 4.40 V was still 98.2%, based on the DVA results shown in Fig. 3 (b). Thus, this indicates that the

dissociation of the graphite anode was not the main reason behind anode deterioration. No significant differences were observed during cycling in the presence or absence of overcharge with respect to the film resistance and capacitance, and solution resistance, as shown in Supplementary Fig. S6.

A possible effect of the overcharging condition on the graphite anode is the deposition of transition metals from the cathode to anode surface. This phenomenon has been reported particularly in manganese-based

cathode materials [32]. A recent paper has reported that the transition metals from nickel manganese cobalt oxide and NCA are also subject to metal dissolution under overcharge conditions and deposited on the anode surface [20]. The cycled anode was analyzed using ICP-AES under the cycling condition of 3.47 V–4.20 V (UCV 4.20 V) or 3.47 V–4.40 V (UCV 4.40 V) to investigate the metals deposited on the anode surface (Fig. 7). Scant deposition of Ni, Co, and Al was observed in the pristine graphite electrode. The transition metal deposited on the anode increases with cycle progression for both UCVs of 4.20 V and 4.40 V. The deposition of only Ni and absence of both Co and Al on the graphite anode was confirmed at an UCV of 4.20 V. The ready deposition of Ni on the anode as opposed to Co or Al in the NCA cathode is similar to the results reported by Watanabe et al. [33]. The deposition of Ni along with Co was detected on a graphite anode cycled at an UCV 4.40 V, which was in good agreement with the results reported by Gilbert et al. [20]. The total amount of metals deposited on the anode surface under different conditions can be ordered as UCV 4.20 V at 100 cycles < UCV 4.20 V at 400 cycles < UCV 4.40 V at 100 cycles < UCV 4.40 V at 250 cycles, which suggests that the overcharging condition promotes the deposition of the transition metals on the anode surface.

Based on the results in Fig. 6 (c), R_{CT-A} evaluated under different conditions can be ordered as UCV 4.2 V at 100 cycles < UCV 4.2 V at 400 cycles < UCV 4.4 V at 100 cycles < UCV 4.4 V at 250 cycles, which also corresponds to the results in Fig. 7. R_{CT-A} increases with an increase in the deposited transition metals on the anode. Contrary results were seen for the interfacial capacitance of the anode, wherein UCV 4.20 V at 250 cycles < UCV 4.40 V at 100 cycles < UCV 4.20 V at 400 cycles < UCV 4.20 V at 100 cycles. Thus, this clearly demonstrates that the amount of transition metals deposited on the anode affects its R_{CT-A} and interfacial capacitance.

The results described above suggest that the UCV difference during charge–discharge cycling affects the elementary electrochemical reactions in the battery cell. A significant difference can particularly be observed in the anode R_{CT-A} and interfacial capacitance. Figs. 1 and 3 (a) show that during cycling, the UCV has no significant effect on the battery capacity till 100 cycles, but always affects the cell capacity after 200 cycles. The anode and cathode capacities Q_A and Q_C , respectively, that were estimated by DVA (Fig. 3(b) and (c)) showed similar trends as observed in the cell capacity fade shown in Fig. 1. The EIS measurement results were on the contrary confirmed to be different. The anode R_{CT-A} and interfacial capacitance values recorded within 100 cycles indicate whether the overcharge condition exists, even though an overcharge during cycling does not affect the cell and anode/cathode capacities. This difference in the anode R_{CT-A} and interfacial capacitance values was due to the deposition of transition metals on the graphite anode, which was evidenced by the ICP-AES measurement (Fig. 7). Some literatures mention that overall impedance rises as the UCV of cycling conditions increase [34–36]. Buchberger et al. reported that the steep capacity decay of overcharged cells is mainly due to the lithium consumptions on anode to form thick SEI layers [34]. The deposition of transition metals on/in SEI layer increases the electronic conductivity of SEI layer, leading to promote side reactions. A gradual coulombic efficiency after 150 cycles at UCV 4.40 V as shown in Figure S2 (c) may reflect this phenomenon. Taking into consideration the fact that SEI on the graphite anode is basically ionically conducting but electrically insulating layer [37], the deposition of transition metals at very early stage of cycling is considered to occur on the graphite surface, which may affect the charge-transfer resistance and interfacial capacitance of graphite anode. If transition metals deposit on the edge plane of graphite anode, R_{CT-A} may increase due to the reduction of reaction area. Further deposition of transition metals may prevent lithium ions from intercalation into graphite anode, leading to the capacity decay of graphite anode. Compared to the capacity decay of anode (Fig. 3 (b)), R_{CT-A} changes at earlier cycles at UCV 4.40 V (Fig. 6 (c)). Therefore, impedance results in this study may detect a very early stage of transition metals' deposition on graphite anode where the deposition does not yet contribute to the

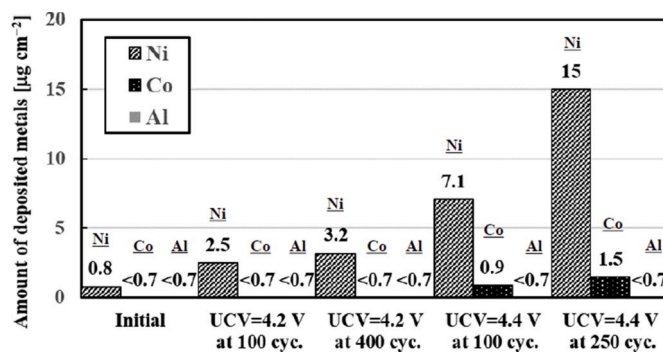


Fig. 7. ICP-AES analysis used to detect the metals deposited on the graphite anode with and without cycling. The cycled graphite anode was prepared by charge–discharge cycling in the 3.47 V–4.20 V (UCV 4.20 V) and 3.47 V–4.40 V (UCV 4.40 V) voltage ranges and cell measurements were recorded after 100, 250, and 400 cycles.

capacity decay of graphite anode in the charge–discharge conditions in this study. We have obtained a certain relationship between R_{CT-A} and deposited amount of Ni on the graphite anode. However, the effect of Co deposition on R_{CT-A} is still unclear since the amount of Co deposition is very low and three conditions out of five conditions in this study showed below detection limit. Further analysis to understand this mechanism is ongoing in current research. The impedance signals change significantly, when an excess of transition metals are deposited on the graphite anode (Fig. 6(c) and (d)). Thus, the detection of the metal deposition on the anode from the dissolution of cathode materials using EIS measurement could be used to predict overcharge-induced serious capacity decay in lithium-ion cells.

In this study, we demonstrate for the first time that the specific impedance parameters change remarkably before a serious capacity deterioration in the battery cell under overcharge cycling conditions. These results indicate that an overcharge-induced serious capacity fade in lithium-ion batteries can be predicted using EIS analysis. Significant impedance changes in the anode R_{CT-A} and interfacial capacitance can predict battery deterioration, which can also be employed to diagnose battery modules (or packs) wherein single cells are connected in series and/or parallel.

4. Conclusion

This study demonstrates for the first time the use of EIS analysis to predict overcharge-induced serious capacity fade in lithium-ion batteries. An NCA lithium-ion cell under overcharge conditions shows a two-stage capacity fade. The capacity gradually decreases as cycling progresses (first stage), and subsequently decreases steeply in the later cycles (second stage). In the first stage, the cell, and anode and cathode capacities are nearly identical, regardless of overcharge. However, a significant difference was confirmed in the metals deposited on the anode surface, due to overcharge-induced dissolution of the cathode active materials. EIS analysis combined with an appropriate equivalent circuit detects in the first stage the metal deposition on the anode, in the form of enhanced impedance signals corresponding to R_{CT-A} and interfacial capacitance. This suggests that serious capacity decay that occurs during the second stage in a lithium-ion battery can be predicted in advance to prevent any cell destruction.

Declaration of competing interest

The authors declare that they have no known competing financial interests or personal relationships that could have appeared to influence the work reported in this paper.

Acknowledgements

This work was supported by the JST-OPERA Program (Grant Number: JPMJOP1612), Japan.

Appendix A. Supplementary data

Supplementary data to this article can be found online at <https://doi.org/10.1016/j.jpowsour.2020.228168>.

References

- [1] G.E. Blomgren, *J. Electrochem. Soc.* 164 (2017) A5019–A5025.
- [2] M. Li, J. Lu, Z.W. Chen, K. Amine, *Adv. Mater.* 30 (2018) 1800561.
- [3] K. Liu, Y.Y. Liu, D.C. Lin, A. Pei, Y. Cui, *Science Advances* 4 (2018), eaas9820.
- [4] D.X. Ouyang, M.Y. Chen, J.H. Liu, R.C. Wei, J.W. Weng, J. Wang, *RSC Adv.* 8 (2018) 33414–33424.
- [5] M.G. Ouyang, D.S. Ren, L.G. Lu, J.Q. Li, X.N. Feng, X.B. Han, G.M. Liu, *J. Power Sources* 279 (2015) 626–635.
- [6] D. Belov, M.H. Yang, *J. Solid State Electrochem.* 12 (2008) 885–894.
- [7] T. Momma, M. Matsunaga, D. Mukoyama, T. Osaka, *J. Power Sources* 216 (2012) 304–307.
- [8] T. Osaka, T. Momma, D. Mukoyama, H. Nara, *J. Power Sources* 205 (2012) 483–486.
- [9] T. Hang, D. Mukoyama, H. Nara, N. Takami, T. Momma, T. Osaka, *J. Power Sources* 222 (2013) 442–447.
- [10] D. Mukoyama, T. Momma, H. Nara, T. Osaka, *Chem. Lett.* 41 (2012) 444–446.
- [11] I. Bloom, A.N. Jansen, D.P. Abraham, J. Knuth, S.A. Jones, V.S. Battaglia, G. L. Henriksen, *J. Power Sources* 139 (2005) 295–303.
- [12] P. Keil, A. Jossen, *J. Electrochem. Soc.* 164 (2017) A6066–A6074.
- [13] K. Honkura, K. Takahashi, T. Horiba, *J. Power Sources* 196 (2011) 10141–10147.
- [14] A.J. Smith, J.C. Burns, X.M. Zhao, D.J. Xiong, J.R. Dahn, *J. Electrochem. Soc.* 158 (2011) A447–A452.
- [15] R.B. Wright, J.P. Christophersen, C.G. Motloch, J.R. Belt, C.D. Ho, V.S. Battaglia, J. A. Barnes, T.Q. Duong, R.A. Sutula, *J. Power Sources* 119 (2003) 865–869.
- [16] C.R. Birkel, M.R. Roberts, E. McTurk, P.G. Bruce, D.A. Howey, *J. Power Sources* 341 (2017) 373–386.
- [17] D. Ansean, M. Dubarry, A. Devie, B.Y. Liaw, V.M. Garcia, J.C. Viera, M. Gonzalez, *J. Power Sources* 356 (2017) 36–46.
- [18] B.P. Matadi, S. Genies, A. Delaille, C. Chabrol, E. de Vito, M. Bardet, J.F. Martin, L. Daniel, Y. Bultel, *J. Electrochem. Soc.* 164 (2017) A2374–A2389.
- [19] E. Flores, N. Vonruti, P. Novak, U. Aschauer, E.J. Berg, *Chem. Mater.* 30 (2018) 4694–4703.
- [20] J.A. Gilbert, I.A. Shkrob, D.P. Abraham, *J. Electrochem. Soc.* 164 (2017) A389–A399.
- [21] T.R. Jow, M.B. Marx, J.L. Allen, *J. Electrochem. Soc.* 159 (2012) A604–A612.
- [22] Z. Ogumi, *Electrochemistry* 78 (2010) 319–324.
- [23] H. Nara, K. Morita, D. Mukoyama, T. Yokoshima, T. Momma, T. Osaka, *Electrochim. Acta* 241 (2017) 323–330.
- [24] A. Funabiki, M. Inaba, Z. Ogumi, S. Yuasa, J. Otsuji, A. Tasaka, *J. Electrochem. Soc.* 145 (1998) 172–178.
- [25] I.A.J. Gordon, S. Grugeon, H. Takenouti, B. Tribollet, M. Armand, C. Davoisne, A. Debart, S. Laruelle, *Electrochim. Acta* 223 (2017) 63–73.
- [26] O. Borodin, D. Bedrov, *J. Phys. Chem. C* 118 (2014) 18362–18371.
- [27] S.S. Zhang, K. Xu, T.R. Jow, *J. Power Sources* 160 (2006) 1403–1409.
- [28] T.P. Heins, N. Harms, L.S. Schramm, U. Schroder, *Energy Technol.* 4 (2016) 1509–1513.
- [29] V.J. Ovejas, A. Cuadras, *Batteries-Basel* 4 (2018) 43.
- [30] N. Ogihara, S. Kawauchi, C. Okuda, Y. Itou, Y. Takeuchi, Y. Ukyo, *J. Electrochem. Soc.* 159 (2012) A1034–A1039.
- [31] G. Liu, H. Zheng, A.S. Simens, A.M. Minor, X. Song, V.S. Battaglia, *J. Electrochem. Soc.* 154 (2007) A1129–A1134.
- [32] C. Zhan, T.P. Wu, J. Lu, K. Amine, *Energy Environ. Sci.* 11 (2018) 243–257.
- [33] S. Watanabe, M. Kinoshita, K. Nakura, *J. Power Sources* 196 (2011) 6906–6910.
- [34] I. Buchberger, S. Seidlmayer, A. Pokharel, M. Piana, J. Hattendorff, P. Kudejova, R. Gilles, H.A. Gasteiger, *J. Electrochem. Soc.* 162 (2015) A2737–A2746.
- [35] H. Zheng, Q. Sun, G. Liu, X. Song, V.S. Battaglia, *J. Power Sources* 207 (2012) 134–140.
- [36] C.T. Love, K. Swider-Lyons, *Electrochem. Solid State Lett.* 15 (2012) A53–A56.
- [37] E. Peled, *J. Electrochem. Soc.* 126 (1979) 2047–2051.